Coherent magnetic structures in self-organized plasmas

F. Pegoraro[1], D. Bonfiglio[2], S. Cappello[2], G. Di Giannatale[2], M.V. Falessi[3], D. Grasso[4], M.Veranda[2]

[1] Dipartimento di Fisica, Pisa University, largo Pontecorvo 3, Pisa, Italy
[2] Consorzio RFX (CNR, ENEA, INFN, Università di Padova, Acciaierie Venete SpA) Corso Stati Uniti 4, Padova, Italy
[3] ENEA, Fusion and Nuclear Safety Department, C.R. Frascati, Via E. Fermi 45, Frascati (Roma), Italy
[4] ISC - CNR and Politecnico di Torino, Dipartimento Energia C.so Duca degli Abruzzi 24, Torino. Italy

Abstract. The concept of Lagrangian Coherent Structures (LCS) has been applied to complex magnetic configurations in plasmas in order to find and characterize their main structural features. LCS allow us to separate regions inside these configurations where field lines exhibit a different kind of behaviour. In the present article we apply this technique to the study of configurations that evolve into a self-organized quasi-single helicity state referring in particular to results obtained in the reversed-field pinch experiment in Padua.

1. Introduction

The concept of Lagrangian Coherent Structures (LCS) was introduced in the context of transport processes in complex fluid flows, see Ref. [1]. In a two-dimensional configuration LCS correspond to special material lines which organize the flow, see e.g. Refs. [2, 3]. Ref. [4] highlights the fact that LCS provide a generalization of the dynamical structures observed in autonomous and periodic systems, such as invariant manifolds, to temporally aperiodic flows. Analogously to the structures in Ref. [2], LCS separate the flow domain into macro-regions inside which trajectories exhibit qualitatively different behaviour over the finite time span which characterize the LCS.

The LCS technique has been used to describe transport processes in a wide range of systems, as detailed in the Introduction of Ref. [4]. In particular in Refs. [4, 5] LCS have been applied to the description of particle transport in magnetized plasmas using the magnetic field lines as a proxy for the structure of the particle trajectories. In Ref. [6] LCS have been used to show how applying boundary magnetic perturbations with different helicities gives rise to transport barriers in a reversed pinch configuration. In the present paper we investigate what kind of information the use of LCS can provide in

the investigation of the magnetic field structure characterizing a self-organized, quasi-single helicity state in the reversed-field pinch experiment in Padua.

This paper is organized as follows. In Sec.2 the Hamiltonian nature of the magnetic field line equation and the relationship with the dynamics of one-dimensional non autonomous dynamical systems are described. In Sec.3 the use of the Poincaré sections and of the LCS is briefly discussed. In Sec.4 we recall the definition of (hyperbolic) LCS. This section does no contain new material but is needed in order to make the present article as self-contained as possible. In Sec.5 we recall the physical context of the present investigation by referring to the process of self-organization of the magnetic field configuration in the RFP in Padua. In Sec.6 we describe the numerical procedure adopted in order to find the LCS and show their structure before and after the plasma self organization into a quasi-single helicity state. Finally conclusions are drawn in Sec.7.

2. Magnetic field as a Hamiltonian system

As is well known [7, 8, 9, 10, 11, 12], due to their solenoidal nature, the field lines of a magnetic field in three-dimensional space that does not vanish within the domain of interest can be described as trajectories of a non-autonomous Hamiltonian system with one degree of freedom. The role of time is played by a spatial coordinate taken to label the points along a field line.

The equivalence between the magnetic field lines and the trajectories of non-autonomous Hamiltonian systems with one degree of freedom has been widely used in the literature by adopting the concepts that are proper of dynamical systems, see in particular Refs. [7, 13, 14].

For the reversed-field pinch configuration considered in Sec.5 a convenient Hamiltonian representation can be obtained by using the so-called "Boozer" coordinates, given by (ψ_t, θ, ζ) with ψ_t the toroidal flux (i.e. the flux of the magnetic field at constant toroidal angle ζ), θ the poloidal angle and ψ_p the poloidal flux:

$$\mathbf{B} = \nabla\psi_t \times \nabla\theta - \nabla\psi_p \times \nabla\zeta. \tag{1}$$

From the definition of magnetic field lines we obtain two equations in Hamiltonian form

$$\frac{\mathrm{d}\theta}{\mathrm{d}\zeta} = \frac{\mathbf{B}\cdot\nabla\theta}{\mathbf{B}\cdot\nabla\zeta} = \frac{\partial\psi_p}{\partial\psi_t}, \tag{2}$$

$$\frac{\mathrm{d}\psi_t}{\mathrm{d}\zeta} = \frac{\mathbf{B}\cdot\nabla\psi_\mathbf{t}}{\mathbf{B}\cdot\nabla\zeta} = -\frac{\partial\psi_p}{\partial\theta}, \tag{3}$$

with $\psi_p(\psi_t, \theta, \zeta)$ the Hamiltonian, ψ_t the canonical momentum, θ the canonical coordinate, and ζ the "time". The choice of ζ as the time variable has been made in analogy to the one made in Refs. [4, 5] in order to allow for a direct comparison. We recall however that in the case of a reversed-field pinch configuration this choice is only possible for $r < r_{rev}$, i.e., in the region inside the radius r_{rev} where the toroidal field reverses.

3. Poincaré sections and Lagrangian Coherent Structures in non-autonomous dynamical systems with one degree of freedom

Non-autonomous periodic systems with one degree of freedom can be conveniently studied by means of the Poincaré section (stroboscopic map) method which makes it possible to reduce the dimensionality of the problem, see e.g. Refs. [15, 16, 17] and to reveal whether the motion of initial conditions is regular or chaotic. Furthermore, invariant manifolds of the map can be used to partition phase space into regions where trajectories have a qualitatively different behaviour on a given time-scale, e.g. bounded or unbounded [18, 19, 20]. These structures play a fundamental role in governing transport processes in non-autonomous dynamical systems and, in particular, they determine the so-called lobe dynamics [21, 22, 23, 24]. Hyperbolic LCS instead, provide a different technique, based on the definition and identification of material lines that are characterized by their property of maximally attracting or repelling nearby material lines, which allows us to generalize these concepts to the study of dynamical systems defined over a finite amount of time without requiring their periodicity. This property of the LCS was exploited in Refs. [4, 5] in order to study the transport of particle in a magnetic configuration evolving in physical time and to ascertain how the appropriately defined LCS depend on the particle velocity.

As indicated by the field line equations (2,3), here we consider magnetic configurations that are periodic along the angle ζ that plays the role of the time. Although the Poincaré map can be used to study the system, the LCS technique makes it possible to further partition the regions characterized by chaotic trajectories into sub-domains where initial conditions have a qualitatively different behaviour on the time intervals which characterize the LCS. Therefore the calculation of the invariant manifolds is not required. We recall that as the time interval that defines the LCS increases these structures converge to the invariant manifolds mentioned above, see Ref. [2], and acquire their typical features.

4. Lagrangian Coherent Structures (LCS)

In this section we recall the definition of LCS that apply to a dynamical system (not necessarily Hamiltonian) in a 2D phase space $\boldsymbol{x}$ with continuous differentiable flow map

$$\boldsymbol{\phi}_{t_0}^{t}(\boldsymbol{x}_0) = \boldsymbol{x}(t, t_0, \boldsymbol{x}_0). \tag{4}$$

Two neighbouring points $\boldsymbol{x}_0$ and $\boldsymbol{x}_0 + \boldsymbol{\delta} x_0$ evolve into the points $\boldsymbol{x}$ and $\boldsymbol{x} + \boldsymbol{\delta} x$ under the linearized map

$$\boldsymbol{\delta} x = \boldsymbol{\nabla} \boldsymbol{\phi}_{t_0}^{t} \, \boldsymbol{\delta} x_0. \tag{5}$$

Given a curve $\gamma_0 = \{\boldsymbol{x}_0 = r(s)\}$ at each point $\boldsymbol{x}_0 \in \gamma_0$ we define the unit tangent vector $\boldsymbol{e}_0$ and the normal vector $\boldsymbol{n}_0$. In the time interval $[t_0, t]$ the dynamics of the system

advects the *material line* γ_0 into γ_t and $\boldsymbol{x}_0 \in \gamma_0$ into $\boldsymbol{x}_t \in \gamma_t$. The linearized dynamics maps the tangent vector $\boldsymbol{e}_0$ into $\boldsymbol{e}_t$ which is tangent to γ_t and is given by

$$\boldsymbol{e}_t = \frac{\boldsymbol{\nabla}\boldsymbol{\phi}_{t_0}^t(\boldsymbol{x}_0)\,\boldsymbol{e}_0}{[\boldsymbol{e}_0\,\boldsymbol{C}_{t_0}^t(\boldsymbol{x}_0)\,\boldsymbol{e}_0]^{1/2}}, \tag{6}$$

where $\boldsymbol{C}_{t_0}^t(\boldsymbol{x}_0) \equiv \left(\boldsymbol{\nabla}\boldsymbol{\phi}_{t_0}^t\right)^T \boldsymbol{\nabla}\boldsymbol{\phi}_{t_0}^t$ is the *Cauchy-Green strain tensor* and ^{T} stands for transposed. This symmetric tensor describes the deformation of an arbitrarily small circle of initial conditions, centred in $\boldsymbol{x}_0$ caused by the flow in a time interval $[t_0, t]$. Let $\boldsymbol{\xi}_{max}$ and $\boldsymbol{\xi}_{min}$ be the two eigenvectors of $\boldsymbol{C}_{t_0}^t(\boldsymbol{x}_0)$ corresponding to the real and positive eigenvalues λ_{max} and λ_{min}. In the case of a Hamiltonian system phase space conservation implies that $\lambda_{min}\,\lambda_{max} = 1$. The curves with tangent vector along $\boldsymbol{\xi}_{min}$ and, respectively, $\boldsymbol{\xi}_{max}$ are called *strain lines* of the Cauchy-Green tensor. In general the mapping does not preserve the angle between vectors and therefore usually the normal vector $\boldsymbol{n}_t$ differs from $\boldsymbol{\nabla}\boldsymbol{\phi}_{t_0}^t\boldsymbol{n}_0$. Using the orthogonality condition $\boldsymbol{n}_0 \cdot \boldsymbol{e}_0 = \boldsymbol{n}_0\boldsymbol{\nabla}\boldsymbol{\phi}_t^{t_0}\boldsymbol{\nabla}\boldsymbol{\phi}_{t_0}^t\boldsymbol{e}_0 = 0$ and inserting Eq. (6) we obtain the expression for $\boldsymbol{n}_t$ which is given by

$$\boldsymbol{n}_t = \frac{\left(\boldsymbol{\nabla}\boldsymbol{\phi}_t^{t_0}\right)^T \boldsymbol{n}_0}{[\boldsymbol{n}_0\,\boldsymbol{C}^{-1}(\boldsymbol{x}_0)\,\boldsymbol{n}_0]^{1/2}}, \tag{7}$$

where $\boldsymbol{C}^{-1}(\boldsymbol{x}_0) = \boldsymbol{C}_t^{t_0}(\boldsymbol{x}_0)$ and the time interval marks have been suppressed as will be the case in the following formulae when not explicitly needed.

We define the *repulsion ratio* $\rho_{t_0}^t(\boldsymbol{x}_0, \boldsymbol{n}_0)$ as the ratio at which material points, in other words points advected by the flow, initially taken near the point $\boldsymbol{x}_0 \in \gamma_0$, increase their distance from the curve in the time interval $[t_o, t]$:

$$\rho_{t_0}^t(\boldsymbol{x}_0, \boldsymbol{n}_0) = \boldsymbol{n}_t\,\boldsymbol{\nabla}\boldsymbol{\phi}_{t_0}^t(\boldsymbol{x}_0)\,\boldsymbol{n}_0. \tag{8}$$

Using the previous definitions, $\rho_{t_0}^t(\boldsymbol{x}_0, n_0)$ can be expressed either in terms of n_0 or of n_t as

$$\rho_{t_0}^t(\boldsymbol{x}_0, n_0) = [\boldsymbol{n}_0\,\boldsymbol{C}^{-1}(\boldsymbol{x}_0)\,\boldsymbol{n}_0]^{-1/2} = [\boldsymbol{n}_t\,\boldsymbol{C}(\boldsymbol{x}_0)\,\boldsymbol{n}_t]^{1/2}. \tag{9}$$

Similarly, the *contraction rate* $L_{t_0}^t(\boldsymbol{x}_0)$ is proportional to the growth in time of the vector tangent to the material line

$$L(\boldsymbol{x}_0, \boldsymbol{e}_0) = [\boldsymbol{e}_0\,\boldsymbol{C}(\boldsymbol{x}_0)\,\boldsymbol{e}_0]^{1/2}. \tag{10}$$

4.1. LCS as maximal repulsion-attraction material lines

Here we adopt the definition of a Hyperbolic LCS as given in Ref. [3]. An LCS over a finite time interval $[t_0, t_0 + T]$ is defined as a line along which the repulsion rate is pointwise maximal. This leads, as shown in Refs. [3, 14], to the following definitions. A line satisfying the following conditions at each point:

$$a) \qquad \lambda_{min} < \lambda_{max}, \quad \lambda_{max} > 1, \tag{11}$$

$$b) \qquad \boldsymbol{e}_0 = \boldsymbol{\xi}_{min} \tag{12}$$

the tangent vector is along the eigenvector associated with the smallest eigenvalue,

$$c) \qquad \boldsymbol{\xi}_{max} \cdot \boldsymbol{\nabla} \lambda_{max} = 0 \tag{13}$$

the gradient of the largest eigenvalue is along the curve, is called a repulsive Weak Lagrangian Coherent Structure (WLCS).
A WLCS which satisfies at each point the additional condition

$$\boldsymbol{\xi}_{max} \cdot \boldsymbol{\nabla}^2 \lambda_{max} \cdot \boldsymbol{\xi}_{max} < 0 \tag{14}$$

is called a repulsive Lagrangian coherent structure. Attractive LCS are defined as repulsive LCS of the backward time dynamics.

5. Self-organized reversed-field pinch configurations

The self-organization process into a global magnetic helical structure has been shown to be a characteristic feature of the plasma dynamics in reversed-field pinches (RFP). This was shown first within 3D nonlinear magnetofluid numerical simulations [25], and it was then observed in high current RFP experiments [26, 27]. This self-organization process is identified with the nonlinear saturation of a single MHD instability [28] which breaks the toroidal axisymmetry, forces the magnetic field lines to wind around a single helical axis and impose a quasi-2D symmetry. This phenomenon allows the chaos, naturally induced by the overlapping of the various magnetic islands associated with the secondary MHD instabilities, to be healed. This brings beneficial effects in terms of increased plasma temperature in the helical core of the plasma, measured in experiments [29].
In Sec.6.2 and 6.3 we will compute the LCS using data obtained from numerical simulations describing the establishment of a helical symmetry. In the present section we recall the numerical MHD model through which these data are obtained and then describe the structure of LCS in two important moments of the plasma evolution: shortly before and soon after the establishment of the helical symmetry.

5.1. MHD model

The following set of dimensionless visco-resistive MHD equations [25, 30]

$$\frac{\partial \boldsymbol{v}}{\partial t} + \boldsymbol{v} \cdot \nabla \boldsymbol{v} = \boldsymbol{J} \times \boldsymbol{B} + \nu \nabla^2 \boldsymbol{v}, \tag{15}$$

$$\frac{\partial \boldsymbol{B}}{\partial t} = \nabla \times (\boldsymbol{v} \times \boldsymbol{B} - \eta \boldsymbol{J}), \tag{16}$$

$$\nabla \times \boldsymbol{B} = \boldsymbol{J}, \qquad \nabla \cdot \boldsymbol{B} = 0, \tag{17}$$

is solved numerically in cylindrical geometry. Here $\boldsymbol{v}$ represent the velocity field, $\boldsymbol{B}$ is the magnetic field and $\boldsymbol{J}$ is the current density. The dimensionless plasma resistivity is denoted by η, while ν indicates the plasma viscosity. Although the plasma pressure is neglected, this model has been shown in Ref. [31] to capture the major physical effects observed in RFP's. In addition it predicted alternative helical magnetic configurations, then observed in the RFX-mod experiment in Padua, that can be obtained by helically modulating the boundary conditions of the radial component of the magnetic field [32, 6].

5.2. Numerical setup

Equations (15-17) are solved in a cylindrical geometry (r, θ, z) with aspect ratio $R_0/a = 4$, where $a = 1$ is the cylinder radius and $2\pi R_0$ the periodicity of the cylinder in the axial direction. Resistivity increases towards the edge while viscosity is uniform. The magnetic Lundquist number $S = \tau_R/\tau_A = 3 \times 10^4$, while the viscous Lundquist number, $M = \tau_\nu/\tau_A = 3 \times 10^1$, here τ_A is the Alfvén time and τ_R, τ_ν are the resistive and viscous time scales respectively. The boundary conditions are no-slip for the velocity field (i.e. $v_\theta(a) = v_z(a) = 0$) and ideal wall for the magnetic field (i.e. $B_r(a) = 0$). The equations are Fourier-transformed in the poloidal and in the axial directions with m for the poloidal number and n the axial number.

5.3. Magnetic field dynamics

The numerical simulation is initiated from an axis-symmetric, unstable equilibrium, with pinch parameter $\Theta = B_\theta(a)/\langle B_z \rangle = 1.6$, that is slightly perturbed. In a first stage, around $t = 600\,\tau_A$ (first vertical blue line in Fig.1), only two relevant MHD modes are present, corresponding to those with the highest growth rate. The largest one has $m = 1$ and $n = 9$, meaning that it creates a structure of islands winding nine times around the axis of the cylinder. The other mode has $m = 1$ and $n = 10$. Despite their small amplitude at $t = 600\,\tau_A$, the magnetic islands associated to the modes interact and a macroscopic chaotic region appears between them (see Fig.2).
As the plasma dynamics evolves, the islands grow increasing the region characterized by chaotic magnetic field lines. At $t = 750\,\tau_A$ (second vertical blue line in Fig.1), the amplitude of the $m = 1, n = 9$ mode becomes so large that the effect of secondary perturbations is negligible and the mode can impress its helical symmetry to the whole configuration.
After $t = 790\,\tau_A$, chaos is strongly reduced in the whole domain, as the $m = 1, n = 9$ mode remains the dominant one, as can be seen in Fig.4 and 5. Interestingly, though the intensity of the secondary perturbations to the helical state continues to increase after $t = 750\,\tau_A$ (see red line in Fig.1), a magnetic chaos healing process occurs despite the presence of remnant spurious modes, contrary to a naïve application of Chirikov criterion [33] reading "the larger the amplitudes and the number of Fourier components, the more chaotic the dynamics". A more detailed description of this simulation can be found in Ref. [34].

6. LCS in the self organizing RFP configuration

lIn this section we apply the definition of the LCS given in Secs.4 and 4.1 to the snapshots, taken at $t = 600\,\tau_A$ and at $t = 750\,\tau_A$ of the evolving RFP magnetic configuration as illustrated in Fig. 1. First we describe the numerical algorithm used and then we discuss the effects of the transition to the quasi single helicity state on the LCS.

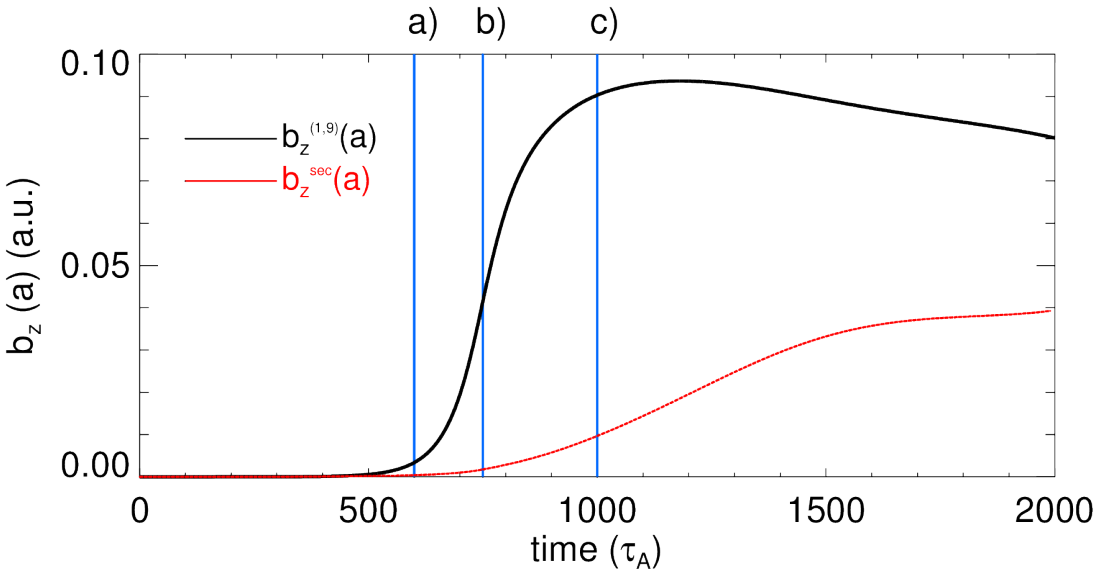

Figure 1: Temporal evolution of the axial component of the magnetic field associated with the dominant mode at the plasma edge (continuous black line). Temporal evolution of the secondary modes is plotted with a red line. The first two blue vertical lines indicate the time of the two snapshots used in the calculation of the Lagrangian Coherent Structures, shown in Fig.2 and 4 respectively before and after the formation of the quasi-helical state. The third vertical blue line at $t = 1000\,\tau_A$ describe a snapshot in which the chaos healing process is completed.

6.1. Algorithm description

In order to compute the LCS, the numerical algorithm requires a grid of initial conditions and the evolution of such initial conditions under the action of a vector field for a time span T. These data are then used to compute the gradient of the flow map $\boldsymbol{\phi}_{t_0}^{T}$ in Eq.(4). Once this matrix is obtained, it is straightforward to compute the Cauchy-Green tensor defined below Eq.(6) and its eigenvalues $(\lambda_{min}, \lambda_{max})$ and eigenvectors $(\boldsymbol{\xi}_{min}, \boldsymbol{\xi}_{max})$ (additional details on the computation of the Cauchy-Green tensor in a general curvilinear geometry are given in the Appendix). Finally, it is possible to construct curves that follow the eigenvectors and to evaluate whether they are or not Lagrangian Coherent Structures by inspecting the validity of the conditions given in Sec.4.1. However, trying to compute the LCS over the whole domain is numerically too demanding. As shown in Ref. [35], a convenient strategy is based on the calculation of the local maxima of the Finite Time Lyapunov Exponents (FTLE) field σ, defined as

$$\sigma(\boldsymbol{x}_0, t_0, t) = \frac{1}{2|t - t_0|} \ln \lambda_{max}(\boldsymbol{x}_0, t_0, t) \tag{18}$$

and the use of the points where the local maxima of the FTLE field are located as the starting points for the integration along the eigenvectors.

The integration of Eq.(12), with initial conditions given by previously selected maxima

of the FTLE field, is performed by using a fourth order Runge-Kutta method.
After the integration, we check whether the curves we have obtained satisfy Eqs.(13, 14). Eq.(13) is the most delicate to verify because most Lagrangian Coherent Structures lie along the ridges of the FTLE field (18) where the gradients of the FTLE field are difficult to compute numerically. Therefore we relax this condition and, instead of $\boldsymbol{\xi}_{max} \cdot \boldsymbol{\nabla}\lambda_{max} = 0$ we impose $\boldsymbol{\xi}_{min} \times \boldsymbol{\nabla}\lambda_{max} = 0$. These two conditions are equivalent since the eigenvectors of the Cauchy-Green tensor are orthogonal. Actually at each point $\mathbf{r}_i$ along the integrated curve we require that $|| \boldsymbol{\xi}_{min}(\boldsymbol{r}_i) \times \boldsymbol{\nabla}\lambda_{\max} ||\leq \mathcal{T}$ where $\mathcal{T}$ is an acceptance threshold. If a point does not fulfil this condition we explore the neighbouring grid points to check whether we are indeed very close to a ridge where the quantity $\nabla\lambda$ may change suddenly direction. The above procedure allows us to find Weak Lagrangian Coherent structures, as defined below Eq.(12). We can further restrict the search of the LCS by applying the condition given by Eq.(14) which ensures that the selected curve is the most repelling material line among neighbouring material lines (for additional details see Ref. [14]).

6.2. LCS before the formation of the quasi-helical state

An investigation of the structure of the magnetic configuration at $t = 600\,\tau_A$,before the formation of the quasi-helical state, has been already presented in Ref. [36] in terms of a different definition of LCS (see Ref. [37]) based on the so called "second derivative ridges" of the FTLE field in Eq.(18). For a discussion of the difference between the two definitions, and of the shortcomings of the definition in terms of the ridges of the FTLE field, see e.g. Sec.V-B of Ref. [4]. As a difference from the case shown in Ref. [36] we adopt the definition of the LCS given in Sec. 4 and compute them with the algorithm, described above in Sec. 6.1 and analysing the differences in the results. To do so, first we consider the Poincaré map and the LCS for the magnetic configuration corresponding to the snapshot at $t = 600\,\tau_A$, Fig.2. We observe that the LCS structures in Fig.2 emanate from hyperbolic points: some of them surround the magnetic islands, separating the chaotic region from a regular one, while others are found in the chaotic region of the magnetic field. We focus on these ones, and show, in Fig.3, that they provide a sharp division between a series of separate regions that cannot be easily located by inspecting the Poincaré plot. In the figure we show that magnetic field lines starting at the opposite sides of an LCS remain separated, at least for a finite time $\bar{\tau}$ (here corresponding to $\sim$ 100 toroidal turns), which is much longer than the dynamical scale (measured by the Alfvèn time, $\bar{\tau}/\ \tau_A \sim 10^3$) and longer than the collisional time scales (measured by the electron-ion collision time $\bar{\tau}/\ \tau_{ei} \sim 10^1$). Thus LCS mark in a clear way barriers to the transport of magnetic field lines. The results shown here and in Refs. [36, 6] indicate that Lagrangian Coherent Structures may provide a good candidate to explain the formation of electron internal transport barriers observed in the reversed-field pinch experiment in Padua (RFX-mod device) [38, 32, 29].
We note here that in Fig.2 and 3 we plotted, for graphical simplicity, only repulsive

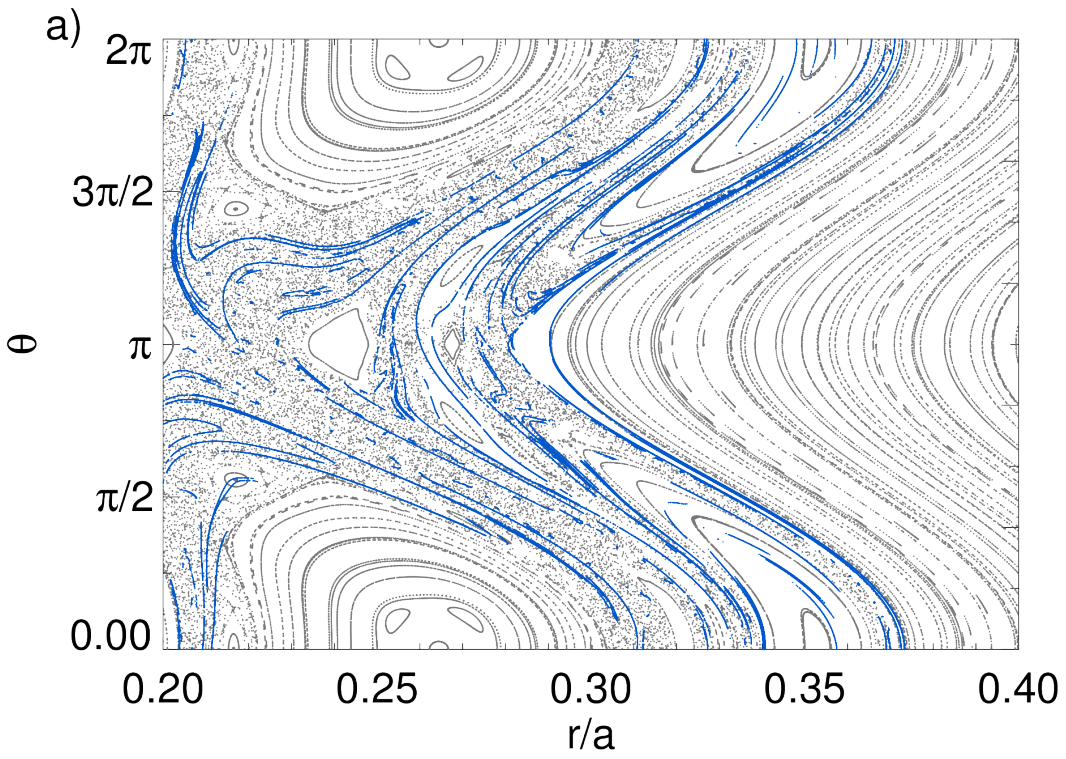

Figure 2: Poincaré map and LCS of the magnetic configuration corresponding to the snapshot taken at $t = 600\,\tau_A$, i.e. before the formation of the quasi-helical state. LCS are overplotted in blue. In this picture we show only the relevant radial region around the $m = 1, n = 9$ helical core (at $r = 0.26\,a$, $\theta = 0$), where a weakly chaotic magnetic field il present.

LCS, while the attractive ones, which have a similar structure, are not shown. A comparison with the results published in Ref. [36] shows that the two methods individuate coherent structures with different precision. The algorithm described in Sec.6.1 detects more continuous structures due to the fact that LCS are here integrated following the eigenvector field, defined in the whole space by Eq.(12), while in the previous work coherent structures were computed as second derivative ridges of the Finite Time Lyapunov Exponents field defined in Eq.(18), which could not always be found in a continuous manner. Furthermore, a comparison between Fig.7 in Ref. [36] and Fig.2 shows that the new algorithm can detect finer LCS. With the new algorithm we can also observe the LCS associated with the separatrix of the dominant $m = 1$, $n = 9$ magnetic island: in particular the one near $r = 0.21\,a$, $\theta \sim 5/4\pi$ in Fig.2 shows the typical lobe structure [39, 40].

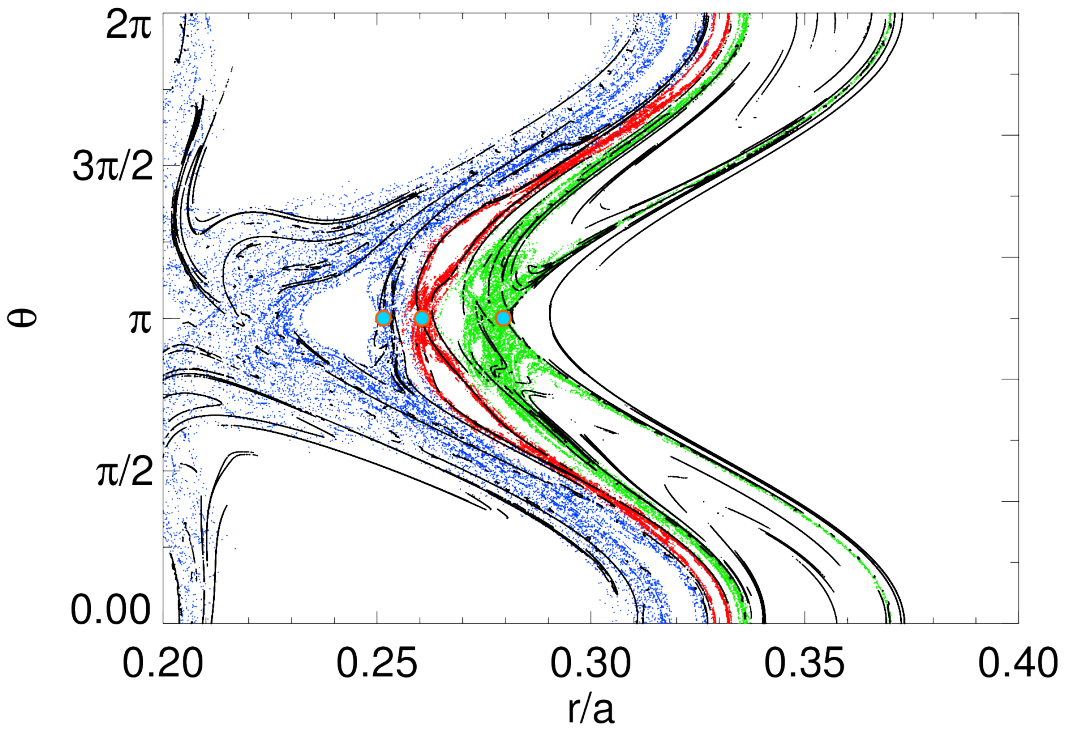

Figure 3: Evidence that LCS divide the space in separated regions. Initial conditions blue dots separated by a LCS remain separated for a finite amount of time.

6.3. LCS after the formation of the quasi-helical state

In Fig.4 we consider the magnetic field configuration at $t = 750\,\tau_A$, right after the formation of the helical state i.e. after the O-point of the magnetic island associated to the $m = 1,\ n = 9$ mode (at $r = 0.26\,a, \theta = 0$ in Fig.2) becomes the main O-point of the helical state. At this time there are no hyperbolic LCS in the region $\pi/2 < \theta < 3\pi/2$, while residual LCS are present only in the chaotic region surrounding the O-point (at $r = 0.5a,\ \theta = 0$) of the new helical structure which is responsible for the healing of magnetic chaos shown at $t = 600\,\tau_A$ in Fig.2.

Obviously, in the region where the Poincaré map exhibits a regular behaviour there is no need to compute the LCS. At $t = 750\,\tau_A$ the pattern is very different since the separatrix of the dominant mode disappears into the new global helical state, a major topological change linked, in the experiments, to beneficial transport properties [29]. At $t = 1000\,\tau_A$ the process of magnetic chaos healing is complete, as can be seen observing the Poincaré plot in Fig.5, characterized by the presence of well conserved magnetic flux surfaces that can be simply described in terms a one-dimensional helical flux function χ. The helical flux function can be defined by the equation $\boldsymbol{B} \cdot \nabla\chi = 0$. For the magnetic field here analysed, characterized by a $h = n/m = 9$ helical symmetry

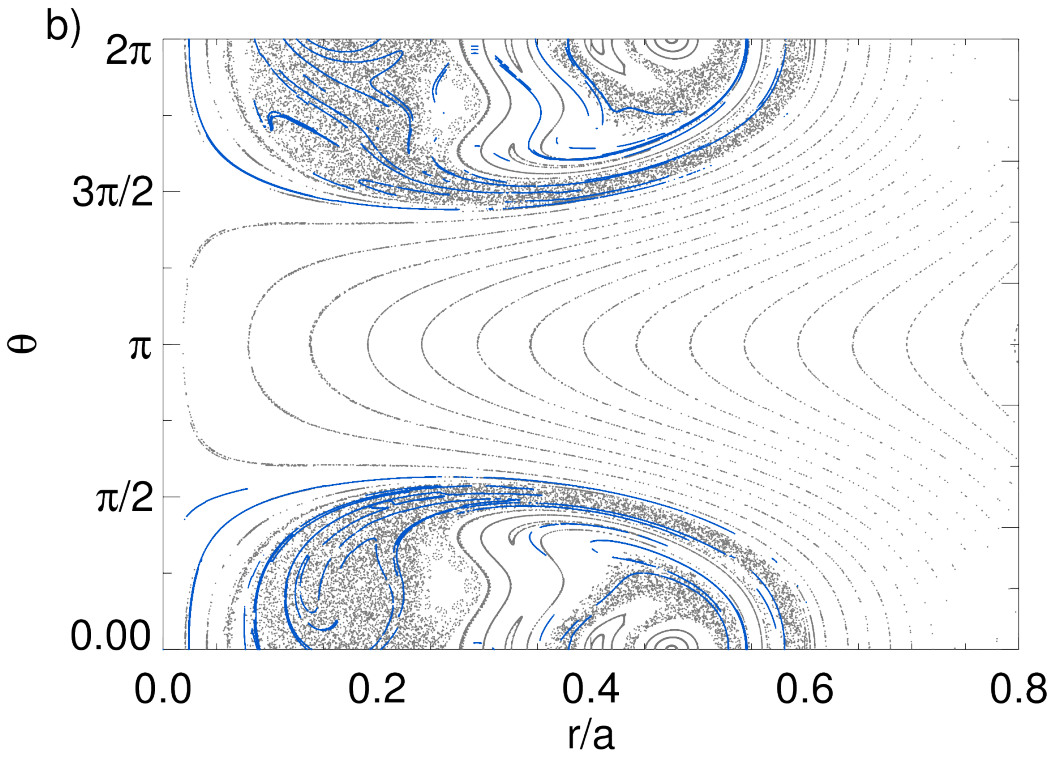

Figure 4: Poincaré map and LCS of the magnetic configuration corresponding to the snapshot taken at $t = 750\,\tau_A$, i.e. after the formation of the quasi-helical state. One can notice that the O-point of the magnetic island, located at $r = 0.26\,a$ in Fig.2, now is the only O-point in the whole domain (helical self-organization). LCS are overplotted in blue. In this picture we show a wider radial region than in the plot of Fig.2, because the helical region occupies a larger plasma volume.

in cylindrical geometry we find:

$$\chi(r,\theta,z) = A_z^{0,0}(r) + \frac{h}{R_0}A_\theta^{0,0}(r) + \sum_m \left(A_z^{m,hm}(r) + \frac{h}{R_0}A_\theta^{m,hm}(r)\right)e^{i(m\theta+hz/R_0)}, \tag{19}$$

with $\boldsymbol{A}$ the vector potential associated the the magnetic field by $\boldsymbol{B} = \nabla \times \boldsymbol{A}$ (we choose $A_r = 0$ as a gauge). Constant χ surfaces, coloured in green in Fig.5, describe correctly the Poincarè plot of the helically symmetric field (in grey).

7. Conclusions

Lagrangian Coherent Structures (LCS) represent a very convenient tool that makes it possible to identify within a complex magnetic configuration macro-regions distinguished by a qualitatively different behaviour of the magnetic field lines.
References [4, 5] have shown in detail how to apply this technique to the study of

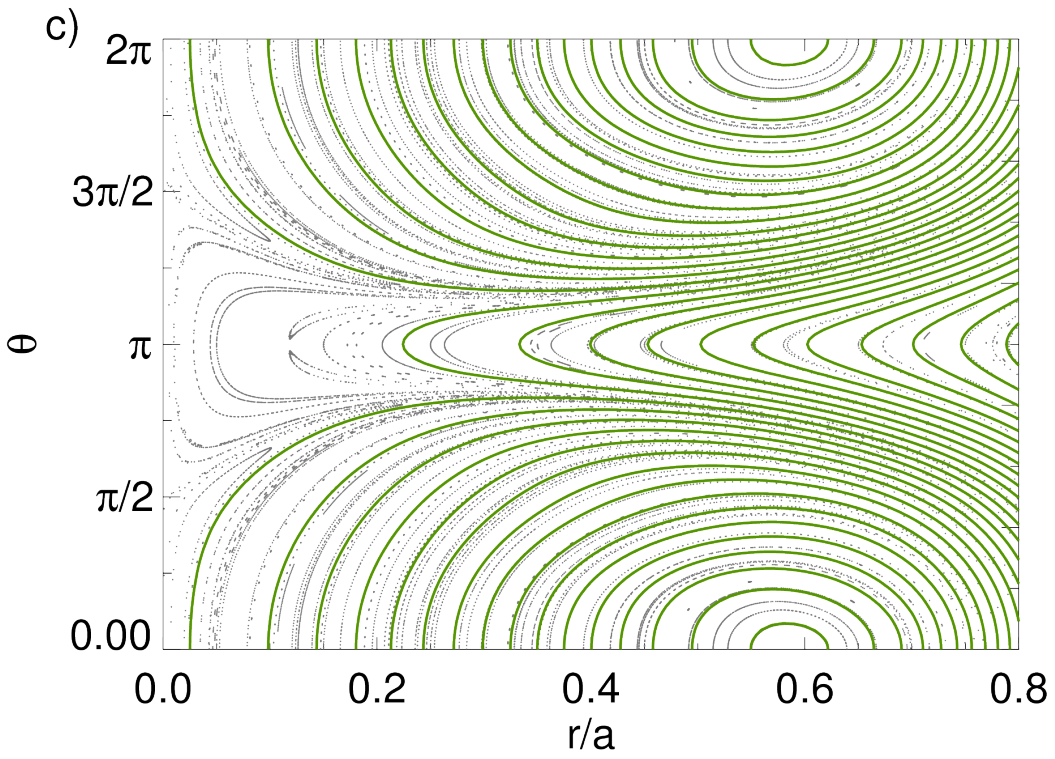

Figure 5: Poincaré map (in grey) of the magnetic configuration corresponding to the snapshot taken at $t = 1000\,\tau_A$, i.e. well after of the quasi-helical state. An LCS computation is not relevant in this case, because the helically symmetric magnetic field can be described in a simpler way by the helical flux function χ, defined in Eq.(19). The the constant χ surfaces are plotted in green.

the growing level of chaoticity in a magnetic configuration with two partly overlapping island chains as the reconnection process proceeds, and have related this process to the modification of the transport of the plasma particles.

In the present article LCS have been applied to a reversed-field pinch configuration that undergoes a process of self-organization and reduction of magnetic chaoticity due to the establishment of a quasi-single helicity state. Following these results and the ones in Ref. [6] we can speculate that LCS correctly describe the structures sustaining the high gradients observed in electron temperature profiles in RFP machines.

Finally, we observe that the role of the LCS in mirroring the changes brought to the plasma dynamics by the magnetic field self-organization into a quasi-helical state, described in the present article, shows that this tool may provide important insight into the transition of a wide range of physical systems from a chaotic to a self-organized state: in fact the process of emergence of self-organized features, representing an essential feature of complex systems, occurs in different physical systems, as exemplified for fluids by the Bénard rolls [41] formed in the presence of thermal convection or by the vortex crystals [42] in systems described by two dimensional Euler equation.

In particular, the formation of transport barriers and improved confinement regimes in fusion plasmas is common to the three fusion configurations tokamak, stellarator, and reversed-field pinch, and several aspects still await satisfactory explanation. By further improving LCS concept application to the different situations, we believe that the technique here reviewed could contribute to a fundamental understanding of transport mechanism in fusion plasmas.

Appendix

We compute the gradient of the flow map $\boldsymbol{\phi} = \phi^i \mathbf{e}_i$ in a general geometry, with coordinates u^i and $\mathbf{e}^i$and $\mathbf{e}_i$ the contravariant and covariant basis vectors, in the tensor form

$$\frac{\partial}{\partial u^i}\ \left\{\phi^j \mathbf{e}_j\right\} \otimes \mathbf{e}^i = A^k{}_\ell\, \mathbf{e}_k \mathbf{e}^\ell = \mathcal{A}^k{}_\ell\, \hat{e}_k \hat{e}^\ell, \tag{20}$$

where summation over repeated indices is understood and in the last equality the unitary basis vectors $\hat{e}^i = \mathbf{e}^i/\|\mathbf{e}^i\|$ and $\hat{e}_i = \mathbf{e}_i/\|\mathbf{e}_i\|$ have been used. Writing the transpose of $\mathcal{A}$ as $\mathcal{A}^T = \mathcal{B}^m{}_k\, \hat{e}_m \hat{e}^k$, the Cauchy-Green tensor becomes

$$\mathcal{C}^m_j\, \hat{e}_m \hat{e}^j = \mathcal{B}^m{}_k \mathcal{A}^k{}_j\, \hat{e}_m \hat{e}^j. \tag{21}$$

Then we specialize Eq.(20) to a cylindrical geometry which is the one used in the Specyl and NEMATO numerical runs reported in Sec.5.2 and compute the eigenvectors of the Cauchy-Green tensor as $\boldsymbol{\xi} = \xi_r \hat{e}_r + \xi_\theta \hat{e}_\theta$ (we recall that in cylindrical geometry $\hat{e}_i = \hat{e}^i$). Finally, we solve the differential equation

$$d\mathbf{l}/ds = \boldsymbol{\xi}(\mathbf{r}), \quad \rightarrow \quad dr/ds = \xi_r,\ d\theta/ds = \xi_\theta/r \tag{22}$$

in a logical grid built as $(r, \theta) \rightarrow (x_{idx}, y_{idx})$, where $r = r_0 + \Delta r\, x_{idx}$, $\theta = \theta_0 + \Delta\theta\, y_{idx}$ and $\Delta r = 1/N_r$, $\Delta\theta = 2\pi/N_\theta$ with N_θ, and N_r the number of mesh points inside the simulation domain $0 \le \theta \le 2\pi$ and $0.20 \le r/a \le 0.45$. In the case of the LCS in Fig.2 we took $N_\theta = 8400$, and $N_r = 4096$.

References

[1] Haller G and Yuan G 2000 *Physica D: Nonlinear Phenomena* **147** 352–370
[2] Haller G 2015 *Annual Review of Fluid Mechanics* **47** 137–162
[3] Haller G 2011 *Physica D: Nonlinear Phenomena* **240** 574–598
[4] Di Giannatale G, Falessi M V, Grasso D, Pegoraro F and Schep T 2018 *Physics of Plasmas* **25** 052306
[5] Di Giannatale G, Falessi M V, Grasso D, Pegoraro F and Schep T 2018 *Physics of Plasmas* **25** 052307
[6] Veranda M, Bonfiglio D, Cappello S, Escande D, Auriemma F, Borgogno D, Chacón L, Fassina A, Franz P, Gobbin M *et al.* 2017 *Nuclear Fusion* **57** 116029
[7] Cary J R and Littlejohn R G 1983 *Annals of Physics* **151** 1–34
[8] Kruskal M D 1952 Some properties of rotational transforms Tech. rep. Forrestal Research Center, Princeton University
[9] Kerst D 1962 *Journal of Nuclear Energy Part C, Plasma Physics, Accelerators, Thermonuclear Research* **4** 253

[10] Gelfand I, Morozov A, Sololev L, Graev M and Zueva N 1962 *Soviet Physics-Technical Physics* **6** 852

[11] Morozov A and Solov'ev L 1966 *Reviews of Plasma Physics* **2** 1

[12] Boozer A H 1981 *Physics of Fluids (1958-1988)* **24** 1999–2003

[13] Borgogno D, Grasso D, Pegoraro F and Schep T 2011 *Physics of Plasmas (1994-present)* **18** 102307

[14] Falessi M V, Pegoraro F and Schep T 2015 *Journal of Plasma Physics* **81** 495810505

[15] Arnold V I, Kozlov V V and Neishtadt A I 2007 *Mathematical aspects of classical and celestial mechanics* vol 3 (Berlin: Springer Science & Business Media)

[16] Wiggins S 1992 *NASA STI/Recon Technical Report A* **92** 28228

[17] Vulpiani A 2010 *Chaos: from simple models to complex systems* vol 17 (Singapore: World Scientific)

[18] Mackay R S, Meiss J and Percival I 1987 *Physica D: Nonlinear Phenomena* **27** 1–20

[19] Meiss J 2015 *Chaos: An Interdisciplinary Journal of Nonlinear Science* **25** 097602

[20] Ottino J M 1989 *The kinematics of mixing: stretching, chaos, and transport* vol 3 (Cambridge: Cambridge University Press)

[21] Wiggins S 2013 *Chaotic transport in dynamical systems* vol 2 (New York: Springer Science & Business Media)

[22] Rom-Kedar V and Wiggins S 1990 *Archive for Rational Mechanics and Analysis* **109** 239–298

[23] Rom-Kedar V, Leonard A and Wiggins S 1990 *Journal of Fluid Mechanics* **214** 347–394

[24] Malhotra N and Wiggins S 1998 *Journal of Nonlinear Science* **8** 401–456

[25] Cappello S and Biskamp D 1996 *Nuclear Fusion* **36** 571–581

[26] Escande D F, Martin P, Ortolani S, Buffa A, Franz P, Marrelli L, Martines E, Spizzo G, Cappello S, Murari A, Pasqualotto R and Zanca P 2000 *Physical Review Letters* **85**(8) 1662–1665

[27] Martin P, Marrelli L, Spizzo G, Franz P, Piovesan P, Predebon I, Bolzonella T, Cappello S, Cravotta A, Escande D, Frassinetti L, Ortolani S, Paccagnella R, Terranova D, Chapman B, Craig D, Prager S, Sarff J, Brunsell P, Malmberg J, Drake J, Yagi Y, Koguchi H, Hirano Y, White R, Sovinec C, Xiao C, Nebel R and Schnack D 2003 *Nuclear Fusion* **43** 1855

[28] Escande D, Paccagnella R, Cappello S, Marchetto C and D'Angelo F 2000 *Physical Review Letters* **85** 3169

[29] Lorenzini R, Martines E, Piovesan P, Terranova D, Zanca P, Zuin M, Alfier A, Bonfiglio D, Bonomo F, Canton A, Cappello S, Carraro L, Cavazzana R, Escande D, Fassina A, Franz P, Gobbin M, Innocente P, Marrelli L, Pasqualotto R, Puiatti M, Spolaore M, Valisa M, Vianello N and Martin P 2009 *Nature Physics* **5** 570

[30] Cappello S 2004 *Plasma Physics and Controlled Fusion* **46** B313

[31] Bonfiglio D, Veranda M, Cappello S, Escande D F and Chacón L 2013 *Physical Review Letters* **111**(8) 085002

[32] Piovesan P, Zuin M, Alfier A, Bonfiglio D, Bonomo F, Canton A, Cappello S, Carraro L, Cavazzana R, Escande D, Fassina A, Gobbin M, Lorenzini R, Marrelli L, Martin P, Martines E, Pasqualotto R, Puiatti M, Spolaore M, Valisa M, Vianello N and Zanca P 2009 *Nuclear Fusion* **49** 085036

[33] Lichtenberg A and Lieberman M 1992 *Regular and Chaotic dynamics* 2nd ed (Springer Science)

[34] Bonfiglio D, Veranda M, Cappello S, Chacón L and Spizzo G 2010 *Journal of Physics: Conference Series* **260** 012003

[35] Onu K, Huhn F and Haller G 2015 *Journal of Computational Science* **7** 26–36

[36] Rubino G, Borgogno D, Veranda M, Bonfiglio D, Cappello S and Grasso D 2015 *Plasma Physics and Controlled Fusion* **57** 085004

[37] Shadden S C, Lekien F and Marsden J E 2005 *Physica D: Nonlinear Phenomena* **212** 271–304

[38] Sonato P, Chitarin G, Zaccaria P, Gnesotto F, Ortolani S, Buffa A, Bagatin M, Baker W, Dal Bello S, Fiorentin P, Grando L, Marchiori G, Marcuzzi D, Masiello A, Peruzzo S, Pomaro N and Serianni G 2003 *Fusion Engineering and Design* **66** 161

[39] Evans T E, Roeder R K W, Carter J A and Rapoport B I 2004 *Contributions to Plasma Physics* **44** 235–240

[40] Punjabi A and Boozer A 2014 *Physics Letters A* **378** 2410 – 2416 ISSN 0375-9601
[41] Chandrasekhar S 1982 *Hydrodynamic and hydromagnetic stability* (Dover)
[42] Schecter D, Dubin D, Fine K and Driscoll C 1999 *Physics of Fluids* **11** 905–914